Materials & Design 224 (2022) 111346

Contents lists available at ScienceDirect

Materials & Design

journal homepage: www.elsevier.com/locate/matdes

Ultrafast-laser powder bed fusion of oxygen-deficient Nb_2O_5 ceramics with highly improved electrical properties

B. Sotillo [a,*], R. Ariza [a,b], P. Fernández [a], J. Solis [b]

[a] Department of Materials Physics, Faculty of Physics, University Complutense of Madrid, Madrid 28040, Spain
[b] Laser Processing Group, Institute of Optics (IO-CSIC), Serrano 121, Madrid 28006, Spain

HIGHLIGHTS

- Optimized ultrafast-laser powder bed processing produces uniform and compact sintered layers of niobium oxide.
- Microstructure and anisotropy of the layers can be controlled with the laser processing conditions.
- Laser processing enables stabilizing a monoclinic oxygen-deficient phase.
- Microstructure and oxygen-deficiency determine the electrical properties of the laser sintered material.
- The sintered material resistivity decreases by more than eight orders of magnitude upon laser treatment.

GRAPHICAL ABSTRACT

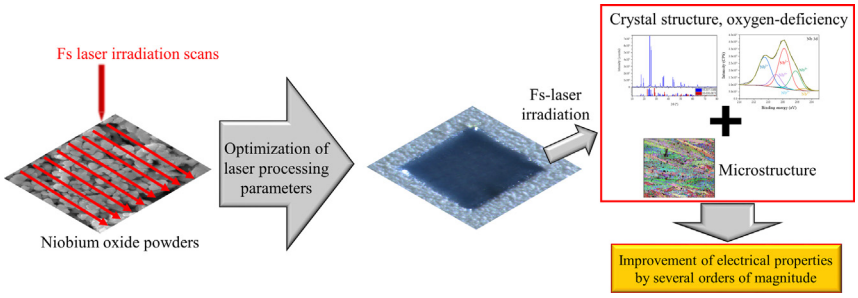

ARTICLE INFO

Article history:
Received 19 July 2022
Revised 2 November 2022
Accepted 3 November 2022
Available online 4 November 2022

Keywords:
Laser powder bed fusion
Niobium oxide
Oxygen-deficiency
Electrical properties

ABSTRACT

In this work, Nb_2O_5 layers with highly improved electrical properties respect to pristine material have been produced by ultrafast-laser powder bed fusion process. The conditions required for producing uniform and compact layers of Nb_2O_5 from powder material have been studied and optimized. It has been established that ultrafast-laser irradiation, performed in air at room temperature, leads to the formation of dense Nb_2O_5 layers with the high temperature monoclinic crystal structure (H-Nb_2O_5) but oxygen deficient. The layers show a preferential crystal orientation with the short axis of the monoclinic structure lying in the structure plane. This preferential orientation can be controlled by the laser irradiation conditions. Anisotropic resistivity has been observed as a consequence of the induced microstructure, while the overall material resistivity is decreased by more than eight orders of magnitude due to the oxygen deficiency. These results indicate that it is feasible to use ultrafast laser processing to promote high-temperature non-stoichiometric niobium oxide phases in a few seconds and with low energy consumption. The highly improved electrical properties of the laser irradiated Nb_2O_5 layers are extremely interesting for different electronic and sensing applications.

1. Introduction

The properties of different polymorphs [1] of Nb_2O_5 have recently caught the attention of the scientific community for different emerging applications as energy storage devices (as batteries

* Corresponding author.
E-mail address: bsotillo@ucm.es (B. Sotillo).

https://doi.org/10.1016/j.matdes.2022.111346
0264-1275/

or supercapacitors). Although the specific capacity of Nb_2O_5 (200 mAh g^{-1}) [2] is relatively modest compared to other materials, it can deliver high power densities without compromising the safety and durability of the device [3–5]. Another important fact is that these oxides can accommodate ions larger that lithium (i.e. sodium and potassium [6]), so they are excellent candidates for the design of energy storage devices beyond the present ion-Li technologies. In photocatalysis [7], Nb_2O_5 can show superior catalytic behavior along with chemical stability, corrosion resistance, non-toxicity and biocompatibility. Niobium pentoxide is also of interest for sensors [8,9] resistive switching devices [10]. The increased absorption of the material could be useful also for electromagnetic absorber materials [11,12].

However, Nb_2O_5 has some important drawbacks that hamper its practical applicability. First, pure Nb_2O_5 has a very low conductivity ($\sigma \approx 10^{-9} S \cdot cm^{-1}$) that hinders the recollection of charge in energy storage devices or decreases the sensitivity in sensors. Second, it has a bandgap in the UV range (about 3.5 eV), preventing its use as photocatalyst in the visible range. In order to increase its conductivity, it has been proposed to add another conductive phase in the fabrication of the electrodes to improve the movement and collection of charge [13]. However, several problems have to be faced, for example the reduction of the amount of active material can lead to a decreased volumetric energy density, along with problems regarding the adhesion of the conductive material to the oxide [14]. Recently, some reviews focusing on the oxygen-vacancy engineering in transition metal oxide semiconductors (for example TiO_2, MoO_3, WO_3 or NiO) for different applications have popped up in the literature [14–18]. For example, in energy storage devices, these types of defects increase the charge carrier density and promote the appearance of extra active sites for redox reactions. On the other hand, for photocatalysis and sensors, they increase surface defects traps that inhibit the recombination of carriers and increase the absorption in the visible range. In the case of Nb_2O_5, different works [4,19,20] point towards the same improved oxide properties (enhanced conductivity) when introducing an oxygen deficiency.

Different strategies are reported in the literature to produce non-stoichiometric oxides with oxygen deficiency. One of the most frequently used is the annealing of the material at high temperature in a reductive atmosphere such H_2 or low-mid vacuum, among others. This strategy has been successfully applied to the formation of non-stoichiometric oxides, for example in TiO_2 [21], MoO_3 [22], WO_3 [23], Nb_2O_5 [24] or Ta_2O_5 [25]. However, this approach suffers of poor controllability and low energetic efficiency (high temperatures are required). Other approaches including electrochemical anodization, hydrothermal reaction, plasma treatment, microwave assisted treatment, solution reduction, flame reduction or doping, have been also proposed [14–18]. In this work we will focus on pulsed laser irradiation, a procedure to induce a reduction in the material that has not been so far frequently used [26–28].

A strategy to obtain metastable or exotic phases of different materials is the irradiation with focused ultrafast laser pulses [29,30]. Focused femtosecond (fs) laser pulses yield peak intensities greater than 10 TW/cm^2, which cause a highly localized energy deposition due to their extremely short duration and micrometric spot size. Such high intensities induce non-linear absorption and non-equilibrium processes with huge heating rates and temperature gradients. They can be thus used to achieve the high temperatures required for sintering niobium oxide ceramics [1]. Moreover, oxygen-deficient Nb_2O_5 phases become more stable at high temperatures [31,32], so ultrafast laser processing may be used to generate oxygen-deficiency in Nb_2O_5 and, as the heating and cooling will be achieved in seconds, avoiding the recovery of stoichiometry by hindering the diffusion of oxygen inside the material. CW-laser irradiation have been used to produce niobates by the sintering of powders with different compositions [33] or UV ns-pulsed laser irradiation has been employed to induce the loss of oxygen at high temperatures [34], but the use of ultrafast laser to sinter and produce an oxygen-deficiency has not been proposed before for niobium oxide materials.

Actually, many of the approaches followed in this work are innovative. CW-Laser powder bed processing has been extensively used for producing different ceramics [35–37]. In most cases additive manufacturing setups include CW- or long pulse duration lasers [38], while the use of ultrafast lasers has been much less exploited [39,40]. Some of the results presented here point towards and improvement of the sintered material ceramic properties. For example, T. Ullsperger et al. [40] observed a reduced melt pool width and a stronger refinement of the microstructure when using ultra-short laser pulses in powder bed selective laser processing.

On the other hand, niobium oxide is a material that can present an exotic behaviour under laser irradiation. Having all these ideas in mind, we have studied the effect of fs-laser irradiation on the sintering process of Nb_2O_5 powders. We have proven that this strategy can produce high quality, uniform across the layer and compact sintered Nb_2O_5 layers (no voids or extended cracks appear) with an oxygen deficiency. More important, we have shown that this strategy can be used to surpass one of the drawbacks of Nb_2O_5 for electrical applications, i.e., the oxygen deficiency leads to decrease of 8 orders of magnitude in the electrical resistivity (or equivalently, an improvement of 8 orders of magnitude in the electrical conductivity). Additionally, we show that the properties of the Nb_2O_5 layers can be tailored by varying the laser-processing parameters, paving the road for using this feasible technology, with a wide range of adaptability, to further design energy storage devices, sensing devices or even in photocatalytic materials on demand.

2. 2. Experimental section

The starting material consist on commercial Nb_2O_5 powders from Alfa Aesar (Puratronic® 99.9985 %, particle size: 400–600 nm). The powders were compacted under a compressive load of 1 T to form disk-shaped pellets. The dimensions of these pellets were 7 mm in diameter and have a thickness of 2 mm (see Fig. 1a, inset). The pellets were thermally treated in a horizontal tubular furnace at 700 °C for 20 h, in order to avoid the pellet to crumble during the irradiation process. After the thermal treatment, the pellets were mechanically polished to obtain a flat surface. The typical morphology of the surface after these processes is illustrated in the SEM image of Fig. 1a, showing that powders are well compacted but not sintered.

Some pellets were sintered for 8 h at 1450 °C (Fig. 1b) in order to have a comparison between the material sintered by thermal treatment and laser irradiation. The sintering conditions were chosen in order to render compact pellets with a minimal porosity. As it can be seen in Fig. 1b, these pellets show a microstructure formed by grains with typical sizes around few tens of microns. This microstructure is commonly observed in thermally sintered ceramics. X-ray diffraction (XRD) and Raman measurements confirm that the starting powders as well as the pellets prepared for laser irradiation are formed by the orthorhombic low temperature polymorph (T-Nb_2O_5), with a minor amount of the monoclinic high temperature polymorph (H-Nb_2O_5). On the other hand, the thermally sintered pellets show a complete transformation of the starting material into H-Nb_2O_5 phase, as expected, since the H phase is the most thermodynamically stable once the material has been treated above 1000 °C [1].

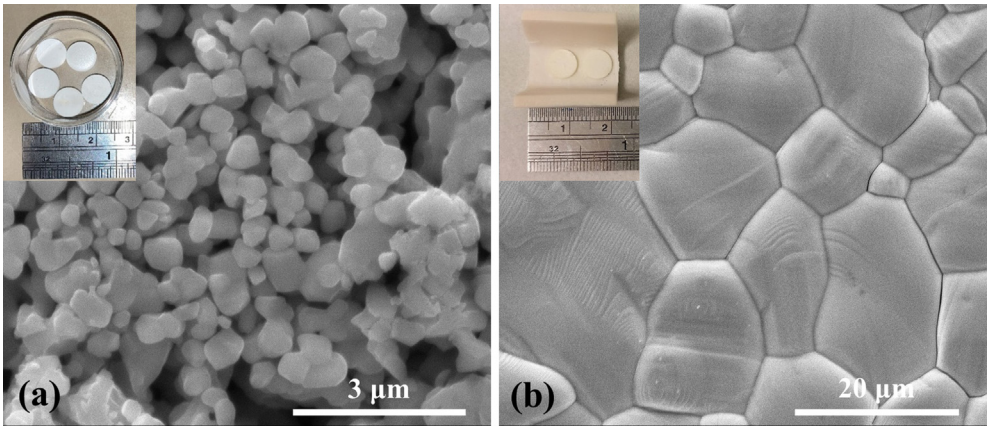

Fig. 1. SEM images of the surface of disc-shape pellets prepared: (a) by thermal treatment at 700 °C for 20 h; (b) by thermal sintering at 1450 °C for 8 h in air.

Femtosecond (fs)-laser irradiation was performed with an Yb-doped, fiber laser (Satsuma HP, Amplitude Systemes) that delivers 350 fs pulses at the fundamental wavelength of 1030 nm. The repetition rate can be varied from 1 kHz to 2 MHz. The details of the irradiation setup can be found elsewhere [41]. The scheme of the final part of the optical path of the setup is shown in Fig. 2a. In brief, the beam coming from a telescope passes through a pinhole of 5 mm and is sent through a galvanometric mirror scanner with an F-Theta lens (f = 100 mm). The spot radius ω_0 of the focused beam at the sample surface was 19.4 µm (waist radius $1/e^2$). A $\lambda/2$ plate is placed before the telescope to control the orientation of the laser linear polarization respect to the scan direction (Fig. 2b). All the laser-processing experiments have been conducted in air atmosphere, i.e., no especial atmosphere is required to process Nb_2O_5.

The different parameters for laser irradiation have been optimized in order to obtain homogeneously irradiated areas while reducing the formation of droplets of ejected material. The pulse energy was varied from 1 µJ to 6 µJ. The laser linear polarization is in most cases kept parallel to the scan direction. The irradiation approach was aimed at producing irradiated layers with a high effective pulse number (Fig. 2b). The effective pulse number in a surface scan ($N_{eff,2D}$) is defined as [42]:

$$N_{eff,2D} = \frac{\pi \cdot \omega_0^2 \cdot RR}{\cdot \Delta}$$

This parameter can be thus controlled in the scan direction by changing the scanning speed (v) and/or the laser repetition rate (RR), and by varying the separation between consecutive scan lines (Δ), as shown in Fig. 2b.

Different characterization techniques have been used to study the properties of the laser-irradiated layers. Scanning Electron Microscopy (SEM) based techniques have been applied: secondary electron mode and electron backscattered diffraction (EBSD). A FEI Inspect or a LEICA 440 SEM have been used for emissive mode measurements. EBSD measurements have been carried out with a Bruker e$^-$Flash Detector coupled to the FEI Inspect SEM working at 20 kV. The analysis of the EBSD data has been performed with the ESPRIT QUANTAX CrystAlign commercial software. Further structural characterization has been performed by means of X-ray Diffraction measurements (XRD), done in a PANalytical Empyrean diffractometer using Cu-Kα radiation, with a step in 2θ of 0.05°.

X-ray photoelectron spectroscopy (XPS) measurements were conducted using a VG Microtech MT 5000 spectrophotometer with a non-monochromatic Mg Kα X-ray source operating at 300 W. The pressure in the analysis chamber was maintained below 10^{-9} Torr. The energy scale was calibrated with an Ag $3d_{5/2}$ (368.3 eV) standard and the peaks have been fitted by Gaussian-Lorentzian mixed functions, after a Shirley background subtraction. The binding energies were calibrated by means of the C 1s band at 285.0 eV (adventitious C).

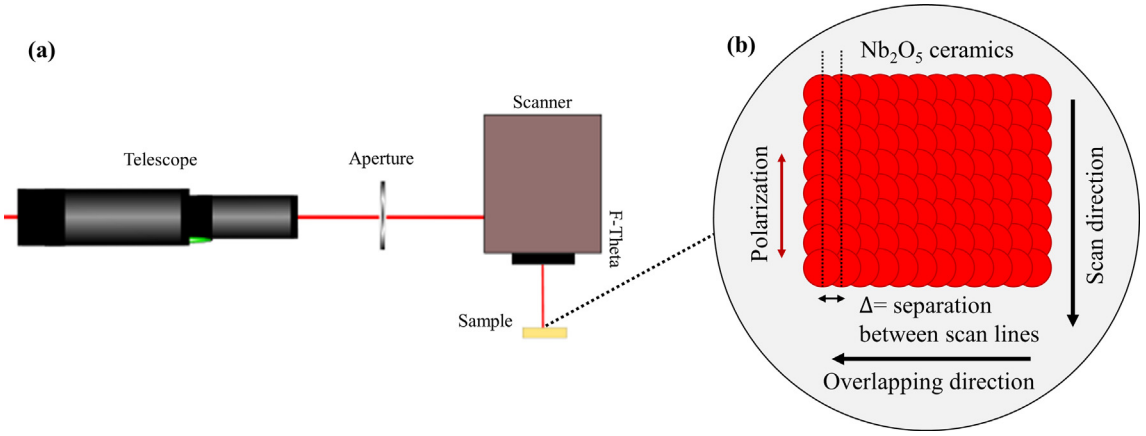

Fig. 2. (a) Experimental setup showing the femtosecond based microfabrication system. (b) Irradiation layout of the Nb_2O_5 ceramics, showing the irradiation parameters including those affecting the effective number of pulses per spot received by the surface.

Micro-Raman (μRaman) measurements were carried out in a confocal microscope Horiba JobinYvon LABRAM-HR, using the 632.8 nm line of a He–Ne laser. The laser was focused onto the sample with a 100× Olympus objective (0.9 NA), and the scattered light was also collected using the same objective (backscattering configuration). The grating used to analyse the signal had 600 l/mm, and the signal was collected with an air-cooled charge coupled device camera (CCD). μRaman spectra were collected and analysed using the Labspec 5.0 software of the confocal microscope.

Finally, electrical resistivity measurements have been performed in an Ecopia HMS-7000 Measurement system. This is a four-point probe system which uses a standard Van der Pauw geometry. For obtaining the electrical resistivity for a isotropic sample, the followed method is described in the NIST webpage [43] and in section S1.1 of supplementary information. More complicate calculations (Montgomery method) have been needed to address the anisotropy of the samples[44], as described in the supplementary information (section S1.2).

3. Results and discussion

3.1. Laser processing parameters

In order to determine the optimal processing conditions to obtain compact and uniform layers, laser parameters have been modified over a broad processing window. The effect of the different laser irradiation parameters (repetition rate, scan speed, pulse energy, separation between scans, etc.) on the Nb_2O_5 powder is described in this section. This is an important step as all these parameters, along with the wavelength, pulse duration, operation mode or beam quality of the laser, will have an impact on the properties of the processed material [38,45,46]. Physical properties of the material will be also taken into account to describe the laser-niobium oxide interaction.

Laser-matter interaction can be divided into three main steps: (1) the initial generation of a free electron plasma, followed by (2) energy relaxation and (3) material modification. As a result of multiphoton ionization and/or tunnelling ionization due to the high peak power of femtosecond laser pulses, a large density of electrons are generated in the focal volume. Avalanche ionization further increases the electron density until a high-density plasma is created. The energy from the electrons is then transferred to the lattice in a time scale longer than the pulse duration, leading to localized heating and eventually the production of permanent modifications of the material. The repetition rate (*RR*) of the laser plays an important role in the heating process of the material. Considering equivalent irradiation parameters, for low-*RR*, the heat is carried away from the focal region by thermal diffusion before the arrival of the next pulse (i.e. pulses act almost independently). A different situation appears for high-*RR*, because the time lapse between pulses is less that the time required by the heat to diffuse away. As a consequence, heat accumulation occurs in the focal volume of the laser and the nearby regions [47]. In this case, the structural modification will be dominated by the heating, melting, and cooling dynamics in and around the focal volume. This division between low and high *RR* is not strict, and the transition between thermal diffusion and heat accumulation will depend also on the material properties. For this reason, in a first round of experiments, the *RR* of the laser was varied from 500 kHz down to 10 kHz, keeping constant the beam scanning speed and pulse energy (0.1 m/s and 6 μJ) in order to study the effects of heat accumulation in the Nb_2O_5 material. It has to be taken into account that the pure Nb_2O_5 has a quite low thermal conductivity (~1 W/m·K) and thermal diffusivity (<1 mm^2/s) [48], so even for low repetition rate values, large heat accumulation effects are expected.

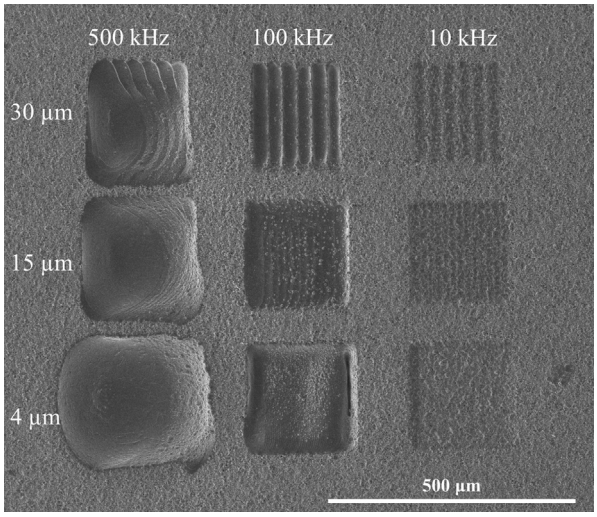

Fig. 3. SEM image showing the effect of varying the repetition rate (*RR*) and separation between scan lines (Δ) on the modification induced by laser irradiation on Nb_2O_5 pellets. Pulse energy (E_p) and scanning speed (v) are kept constant (6 μJ and 0.1 m/s, respectively).

Illustrative results of the effect of varying the *RR* are shown in Fig. 3. For a RR of 500 kHz, the energy deposited into the material is too high and the modification of niobium oxide is accompanied by a large extent of material removal, leading to a clearly visible depression in the irradiated area. This RR is thus too high for the production of a uniform layer. On the other hand, for 10 kHz, the energy accumulation in the material is not enough for appreciable modifications to occur across all the irradiated region, and the resulted layer is neither sintered nor compact. By varying the repetition rate between these two values, we have observed that a RR in the range of 100 kHz is optimal for producing uniformly sintered layers of Nb_2O_5.

Another important parameter in the irradiation strategy is the separation between scans (Δ), which was varied from 4 to 30 μm. As it can be seen in Fig. 3, for 100 kHz, when the separation between scans is larger than the laser spot radius at the surface (19.4 μm), the formed trenches are separated by regions of non-modified material. The intensity distribution of the laser at the surface follows a Gaussian profile, so the depth profile of these separated trenches is related to this intensity distribution. For Δ = 15 μm (slightly smaller than the laser spot at the surface) the vertical trenches are still visible. It is necessary to produce a high overlapping between consecutive scans (Δ = 4 μm) to obtain a uniform roughness distribution in the irradiated area, as it can be seen in Fig. 3 for RR = 100 kHz and Δ = 4 μm.

Pulse energy and scanning speed also have an impact in the homogeneity of the formed layer. High values of pulse energy induce a large ejection of material from the irradiated area (as shown in Fig. 3), whereas low values lead to isolated and non-connected areas of modified material (Fig. 4a). The same effect is observed when the scan speed is increased (Fig. 4b). From visual inspection, homogeneous and continuous layers were obtained when the pulse energy is in the range of 3.5 – 4.5 μJ and the scanning speed is in the 0.1 – 0.2 m/s range (which corresponds to $N_{eff,2D}$ values 297 and 148, respectively). It has also been observed that performing two consecutive area scans reduces the density of droplets and the formation of micro-cracks, although they cannot be completely avoided [39] (Fig. 4c). However, a further increase of the number of scans on the same region only induces the deformation of the irradiated layer and the formation of waves on the surface.

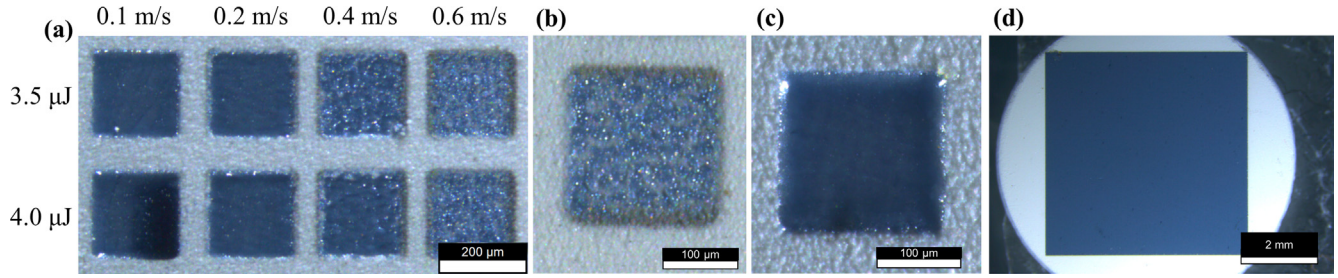

Fig. 4. Optical microscopy images (real colour) of fs-laser irradiated Nb_2O_5 pellets: (a) effect of the variation of scanning speed for two pulse energies; (b) irradiation performed at *RR* = 100 kHz, Ep = 3.5 µJ, v = 0.6 m/s, Δ = 4 µm, showing non-connected regions of modified material; (c) irradiation performed with optimized laser irradiation conditions: *RR* = 100 kHz, Ep = 3.5 µJ, v = 0.1 m/s, Δ = 4 µm, two consecutive scans; (c) Irradiation performed with the same parameters as (b), but covering the full available area of a disc-shape pellet (7 mm diameter).

The laser-irradiation parameters in this processing window (*RR* = 100 kHz, Ep = 3.5 – 4.5 µJ, v = 0.1 – 0.2 m/s, Δ = 4 µm) have been selected to perform further studies regarding the microstructure, composition, and electrical properties of the irradiated layers. It has been checked that the results are reproducible when working with these selected parameters. By using the parameters in the optimal processing window it is possible irradiating in a few seconds homogenous areas as large as 5 mm × 5 mm (the largest area that can correctly be fitted on the Nb_2O_5 pellets), as it can be seen in Fig. 4d.

A closer inspection of the surface of the irradiated regions has been performed using a SEM microscope. In Fig. 5a the edge of the irradiated layer is shown, where a clearly visible difference between the irradiated (left part of the image) and the non-irradiated material (right part) can be appreciated. The edges between the modified and non-modified material are sharp and well defined (Fig. 5a-b), with a clear difference between the sintered material and the pristine powders. A sharp boundary between irradiated and non-irradiated material was expected due to the use of an ultrafast laser [40].

The irradiated layer is dense without large size pores. Some micro-cracks are still visible on the surface, possibly related to a difference in the coefficients of thermal expansion of the upper and lower materials[39]. Nevertheless, if the cross-section of the layer is inspected (Fig. 5b), it is possible to see that the micro-cracks do not extend along the thickness of the densified layer. Rather, they seem to be quite superficial. The cross-section images confirm no pores are present inside the sintered layer, something relevant, as pores formed inside the sintered material will be detrimental for the ceramic properties. It has also been confirmed that micro-cracks and droplets are superficial as they are easily removed by a soft mechanical polish, as shown in the image in Fig. 5c. The avoiding of cracks formation in the densified layer may be related with the mechanical properties of niobium oxide (Young's modulus, coefficient of expansion, strength) [49], as well as to the processing strategy and the formation of the oxygen-defective phase. In the first case, the generated thermal stresses are not sufficient to overcome the strength of the material. With the processing strategy, a second swept of the laser on the layer repair the cracks that may form during the first scan. Finally, the oxygen-deficient phase is expected to have an improved thermal conductivity, reducing the possibility of thermal shock in the layer.

Cross-sectional images have been used to measure the thickness of the sintered layers in the optimal processing window, as presented in Table 1. In all cases, the thickness is in the range of a few microns. It has been observed that the thickness increases with the pulse energy and reduces when the scan speed is raised. This is, if the fluence ($2E_p/\pi\omega_0^2$) increased, more energy per unit area is delivered, so a higher volume of the material can be affected by the increase of temperature. A larger variation in the thickness is observed by varying the effective pulse number, $N_{eff,2D}$. A higher value of pulse overlapping turns into a higher heat accumulation and a larger volume of laser-modified material [47]. Non-uniform layers outside the optimal processing window consist on isolated islands (see for example the higher speeds in Fig. 4a) of transformed material, with a depth of less than 10 µm. Micrometric-size Nb_2O_5 material has been successfully incorporated in energy storage devices [5,50], so the laser-processed material would be useful to form electrodes with different 3D networks [51].

3.2. XPS measurements

In the optical microscope images of Fig. 4, along with the formation of a compact layer of sintered niobium oxide, it is clearly visible that the material presents a change in colour from white to blue-grey. This colour change in transition metal oxides, and especially in niobium oxide [1,52], has been typically associated with the appearance in the lattice of metal cations with lower oxidation

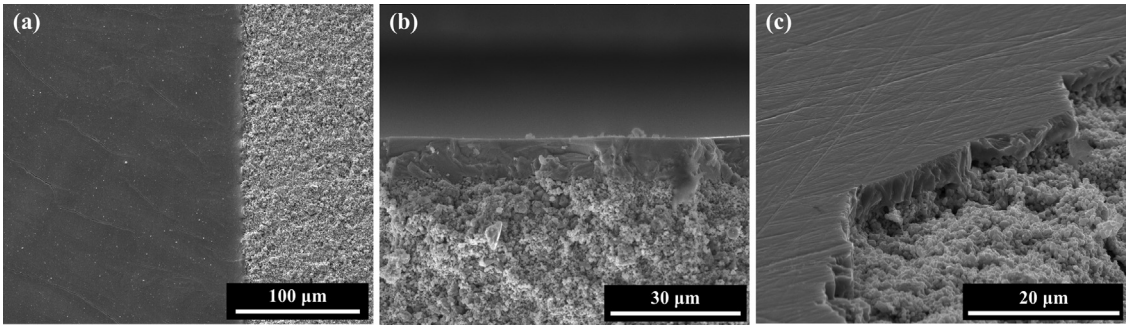

Fig. 5. SEM images of Nb_2O_5 laser-irradiated layers: (a) top view of the layer's edge (on the right a part of the non-processed material is still visible); (b) cross-section of the layer; (c) tilted view of the layer after soft mechanical polish.

Table 1
Measured thickness of laser-sintered niobium oxide layers for different laser irradiation parameters.

Laser parameters (for RR = 100 kHz)	$N_{eff,2D}$	Fluence (J/cm^2)	Layer thickness (μm)
E_p = 3.5 μJ; v = 0.1 m/s; Δ = 4 μJ; 2 scans	296.8	0.59	9
E_p = 4.0 μJ; v = 0.1 m/s; Δ = 4 μJ; 2 scans	296.8	0.67	10
E_p = 4.0 μJ; v = 0.2 m/s; Δ = 4 μJ; 2 scans	148.4	0.67	6
E_p = 4.5 μJ; v = 0.2 m/s; Δ = 4 μJ; 2 scans	148.4	0.76	7

state and oxygen vacancies. A low concentration of oxygen vacancies produces the formation of donor levels in the bandgap of the material [53]. Also, it induces a change in the oxidation state of the metal, leading to more electrons available for the conduction due to the unpaired d-electrons from the lower oxidation state niobium ions (in Nb_2O_5, niobium ions are mainly found in the form of Nb^{5+}). In presence of a high oxygen-vacancy concentration, changes in the oxide crystal structure and metal coordination polyhedra can appear to accommodate this deficiency [53], leading to further modification of the band structure of the material.

As it has been said before, stoichiometric Nb_2O_5 will have niobium ions mainly found in the form Nb^{5+}. Once oxygen deficiency is introduced in the material, the oxidation state varies to Nb^{4+} or Nb^{2+}, as less oxygen is available in the lattice to form bonds. In this context the determination of Nb oxidation state from XPS measurements is a good indicator to monitor the oxygen content or deficiency. In order to have a reference, the same measurements have been performed on pellets of untreated material and on pellets of sintered Nb_2O_5 at 1450 °C. For all the samples, O 1s, C 1s and Nb 3d bands are detected (Fig. S1a). No important differences are visible between the Nb 3d bands of the three samples. At least no differences that can explain the change in colour of the irradiated Nb_2O_5, as it can be seen when comparing the bands in Fig. S1b (non-irradiated material) and Fig. 6a (laser-irradiated layer). Previous studies performed on different types of niobium oxides [54,55] have pointed out that an oxide surface layer with composition closer to stoichiometric Nb_2O_5 (most stable form of niobium oxide) is always formed due to the contact of the surface metal atoms with the air atmosphere. In the case of laser irradiated Nb_2O_5, it is possible, due to the high temperatures reached by the material in the irradiation process, that the superficial layer, in contact with air atmosphere, is mainly formed of stoichiometric oxide. It must be considered that XPS provides compositional values corresponding to an exponentially decaying interaction in the near-surface region (2–3 nm depth) while the stoichiometric surface oxide layer can me much thicker.

In order to remove this superficial oxide layer, a gentle mechanical polish of the surface of the irradiated layer (as shown in Fig. 5c) was performed prior to the XPS measurements, along with an Ar-bombardment cleaning. The complete process is described in the Supplementary Information (section S2). The XPS Nb 3d bands obtained after this procedure, and associated to the inner region of the layer, are shown in Fig. 6b. Whereas the bands associated with Nb^{5+} in Nb_2O_5 are still present (located at 210.5 and 207.8 eV), Nb^{4+} related bands increase (at 208.9 and 206.2 eV) and bands adscribed to Nb^{2+} (at 207.7 and 205.0 eV) are clearly visible (see Fig. 6b). The increase and/or appearance of the bands related to Nb^{4+} and Nb^{2+} is an indication that less oxygen is available in the lattice to form bonds, and that the oxidation state of the cations is reduced.

The O 1s band for the inner region of the layer is presented in Fig. 6c. It is composed by two bands (O_1 and O_2), typically attributed to lattice oxygen anions in the oxide matrix and to oxygen vacancies formed in the lattice [56], respectively. The O 1s band present slighter changes when compared to the XPS spectra recorded on the superficial layer (Fig. S1c). The main difference is the shift of both bands towards higher binding energies in the inner material (from 530.1 eV towards 530.9 eV and from 531.9 eV towards 532.5 eV, respectively). These shifts can be related to the formation of more Nb^{4+}-O bonds and Nb^{2+}-O at the expense of Nb^{5+}-O bonds [57], in agreement with the increase of Nb^{4+} and Nb^{2+} in the Nb 3d band. It is important to point out that the O_2 band, associated to oxygen vacancies, do not increase (see Table 2), despite the increase of Nb^{4+} and Nb^{2+} signals. This can be related to the appearance of Wadsley-Roth shear defects, a common defect in Nb_2O_5 that tends to compensate the formation of oxygen vacancies [4].

The quantification of the surface composition for the laser-irradiated layer was computed from the area under the XPS bands, and is shown in Table 2. The ratio O:Nb is decreased in the inner laser-irradiated material (O:Nb = 2.44), confirming that the material formed is non-stoichiometric with a clear oxygen deficiency. On the other hand, the superficial oxide layer formed during laser-irradiation in contact with air has a higher O:Nb ratio (O:Nb = 2.65).

3.3. XRD measurements

XRD measurements have been performed in order to study the crystal structure of the different samples and analyse the modifica-

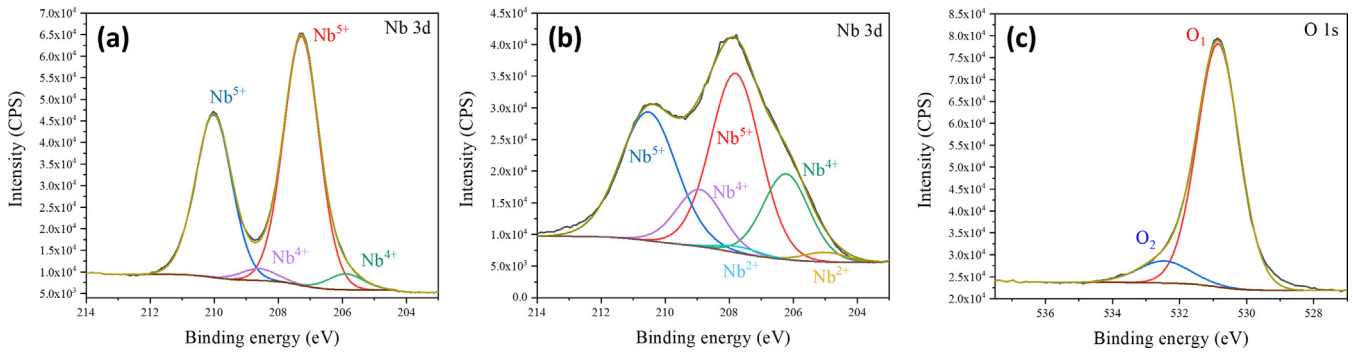

Fig. 6. XPS spectra recorded on the laser-irradiated Nb_2O_5 layers: (a) Nb 3d band of the as-prepared layer. (b) Nb 3d band and (c) O 1s band both after removal of the stoichiometric superficial oxide layer by gentle polishing and Ar-bombardment (see text).

Table 2
Surface chemical composition of the laser-irradiated layer, derived from the XPS spectra. The detected C 1s signal is related to adventitious carbon on the surface of the sample. The composition associated to the different XPS bands is also shown.

	Oxide superficial layer	Inner laser-irradiated material
XPS band	Atomic %	
O 1s (total)	**60.3**	**64.1**
O_1 band	52.5	57.6
O_2 band	7.8	6.5
C 1s (total)	**17.0**	**9.7**
285.0	16.6	7.7
286.7	2.7	1.4
288.9	1.7	0.6
Nb 3d (total)	**22.7**	**26.3**
Nb(V) $3d_{5/2}$	12.8	10.0
Nb(V) $3d_{3/2}$	8.5	8.1
Nb(IV) $3d_{5/2}$	0.8	4.4
Nb(IV) $3d_{3/2}$	0.6	3.0
Nb(II) $3d_{5/2}$	–	0.5
Nb(II) $3d_{3/2}$	–	0.3

tions introduced in the material by fs-laser irradiation. First, the data collected for the non-irradiated pellets are shown in Fig. 7a. Most of the detected diffraction maxima are ascribed to the orthorhombic T-Nb_2O_5 with ICDD card no. 00-030-0873. Some lower intensity maxima can be related to the monoclinic H-Nb_2O_5 with ICDD card no. 00-037-1468. The diffractogram is the same as the one recorded on the original commercial powders, confirming that the thermal treatment performed at 700 °C for 20 h has only increased the compaction of the powders without altering the crystal structure.

The XRD measurements performed on the laser-irradiated layer show clearly that the material has undergone a crystal phase transition (Fig. 7b). In fact, the diffraction maxima detected are in good agreement with the position of the maxima of monoclinic H-Nb_2O_5. The diffractogram has the same maxima as those detected in the sintered pellet at 1450 °C (Fig. 7c). For both cases, no diffraction maxima related to the orthorhombic T-Nb_2O_5 or to other niobium sub-oxides are visible. Laser irradiation of niobium oxide powders is thus able to transform the material into the high temperature crystal structure (this means, 100 % of monoclinic phase), which typically appears for annealing temperatures above 1000 °C, but with a very low energy consumption compared to a thermal annealing process.

A slight shift towards higher 2θ of some maxima in the irradiated layer is detected, which can be related to a slight change of the lattice parameters. The main difference is found in the relative intensity of some maxima: some of them have higher intensity than expected from the JCPDS card and respect to other maxima. This behaviour is typically related to the presence of a preferential orientation or texture in the layer, which has been confirmed using EBSD measurements.

The combination of XRD results with XPS measurements allow to conclude that the niobium oxide produced by laser irradiation has a defective monoclinic H-Nb_2O_5 crystal structure. The rapid rate of heating and cooling induced by the fs-laser irradiation is inducing this high temperature crystal structure of Nb_2O_5 with intrinsic defects, mainly oxygen deficiency with the subsequent formation of Nb^{4+} and Nb^{2+} species. At high temperatures, oxygen-deficient phases become more stable, depending on the partial pressure of oxygen [31,32]. In our experiment, only the surface is in direct contact with an atmosphere containing oxygen. The rapid cooling rate prevents the diffusion of oxygen inside the layer, stabilizing the high temperature defective crystal structure at room temperature. Further protection of this oxygen-deficient material is achieved by the superficial stoichiometric oxide layer formed (as above described in the XPS measurements).

3.4. μRaman measurements

μRaman measurements have been used to get further information about the material structure but adding spatial resolution. For Nb_2O_5, the crystal structure can be seen as a weave of corner or side-linked NbO_6 polyhedra (mainly octahedra). Therefore, the Raman spectrum of niobium pentoxide can be divided into different frequency (ν) regions, associated with different types of vibration of the NbO_6 polyhedra in the crystal lattice, as indicated in Table 3.

The bands in Table 3 can be identified in the Raman spectra recorded on the starting pellets, sintered pellets and laser irradiated layers as shown in Fig. 8. The differences observed in the position and shape of the Raman bands are related with structural changes of the Nb_2O_5. In Fig. 8a, the comparison of the Raman spectra recorded on the cross-section of the irradiated layer and the non-irradiated material is presented. Two main differences are observed. First, the bands become sharper for the irradiated layer. Second, the band with the maxima located between 600 and 700 cm^{-1} is shifted towards lower wavenumber. These modifications in the Raman spectra appear when Nb_2O_5 changes from a low-temperature crystal structure (as orthorhombic T-Nb_2O_5) to monoclinic high temperature structure (H-Nb_2O_5) [63]. These observations are in agreement with the change in the crystal structure observed in XRD, and confirms that the laser-irradiation is able to produce a layer of high-temperature crystal structure of Nb_2O_5 material.

More information can be extracted from the comparison of the Raman spectra of the irradiated layer and the high temperature sintered ceramic (Fig. 8b). In contrast with the results obtained

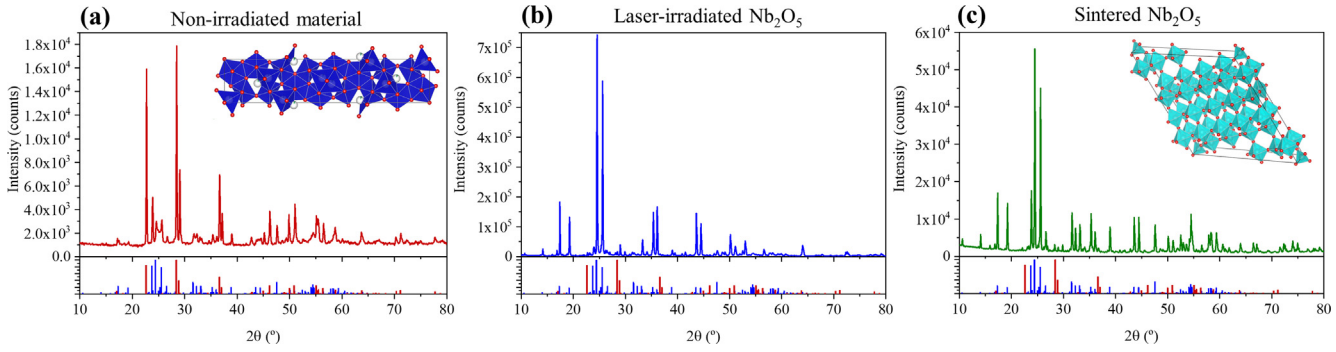

Fig. 7. XRD measurements performed on different samples: (a) non-irradiated material: (b) laser-irradiated layer; (c) sintered material at 1450 °C. The tabulated diffraction maxima for ICDD cards no. 00-030-0873 (red bars) and no. 00-037-1468 (blue bars) are indicated below each diffractogram. The insets shown the crystal structure of (a) orthorhombic T-Nb_2O_5 and (b) monoclinic H-Nb_2O_5, plotted using VESTA software[58].

Table 3
Origin of the Raman modes in Nb_2O_5.

Wavenumber (cm^{-1})	Origin
$\nu < 200\ cm^{-1}$	External lattice vibrations [59]
$200\ cm^{-1} < \nu < 450\ cm^{-1}$	Bending-related modes in the NbO_6 units [60,61]
$450\ cm^{-1} < \nu < 900\ cm^{-1}$	Stretching-related modes in the NbO_6 units [60,61]
$993\ cm^{-1}$	Symmetric stretching modes of the terminal bonds of Nb = O [60,61]. Shear planes [62]

with XRD (Fig. 7), clear differences can be observed between the Raman spectra of both samples, however the Raman modes observed in both samples may be ascribed to the monoclinic phase. The main differences between the spectra from both samples are the width and intensity that, as well as the slight differences in peak positions, can be attributed to stresses due to lattice distortion or defects. More interesting is the shift or asymmetric broadening of some peak towards lower wavenumber. These effects are clearer for the band located at 993 cm^{-1} (Fig. 8c), as it is sharper than the others. This band is shifted from 993 cm^{-1} towards 990 cm^{-1} in the irradiated layer, and the broadening is observed towards lower wavenumber. These behaviour in the Raman spectra have been previously observed in other metal oxides [64–66], and have been related to the formation of oxygen vacancies. In addition, a shift towards lower wavenumbers is related to a tensile stress or an increase in the bond length, which would be in agreement with the formation of more Nb^{4+}-O bonds (~205.7 pm) and Nb^{2+}-O (~210.5 pm) bonds at the expense of Nb^{5+}-O bonds (~199.0 pm) [57,67]. In agreement with these previous works and with the performed XPS measurements, Raman studies confirm the appearance of a strong oxygen deficiency in the Nb_2O_5 laser-irradiated layer. Further information about the microstructure of the layer would be difficult to extract from these measurements due to the complexity of the Raman spectra. A further insight on structural properties will be acquired with the EBSD results presented in the next section.

3.5. EBSD measurements

As it has been described in the XRD measurements, some texture or preferential orientation is detected in the laser processed layers. EBSD measurements (Fig. 9) enable to achieve a deeper insight in the microstructure of the laser-irradiated layer. Inside the SEM chamber, the sample has been oriented placing the edges of the irradiated areas parallel to the XY axis of the microscope, whereas the Z axis will be perpendicular to the layer plane. These axes are indicated in the scheme in Fig. 9a. All the EBSD measurements are referred to this reference system.

Along with the reference system, in Fig. 9a inverse pole figures (IPF) for X, Y and Z axes recorded over an area of 440 × 440 μm^2 on an irradiated layer are presented. In these figures, the density distribution of the inverse poles gives information about the mean crystal orientation of the layer. For this sample, the scan direction is parallel to the Y-axis and the overlapping direction is along X-axis. According to the legend shown in Fig. 9b, the [001] direction (which is the shortest axis (*c*-axis) in the monoclinic crystal structure in Fig. 9c) is mainly located in the plane of the irradiated layer, and typically closer to the X-axis that to the Y-axis. This is, it appears mainly parallel to the overlapping direction and perpendicular to the laser scan direction and/or laser polarization. As observed in IPF for Y and Z, the other two crystallographic axes, *a* and *b*, are found randomly rotated around *c*-axis.

Further information about the microstructure can be obtained by plotting the IPF maps for each axis of the sample. Each point/pixel in the IFP is associated to a colour value following the legend shown in Fig. 9b. The results for an irradiated region of 0.2 × 0.2 mm are shown in Fig. 9d. First, on the right of the SEM image, the pattern quality map is shown. In this map, for each pixel, a grey scale code is assigned depending on the contrast and sharpness of the diffraction pattern. Darker pixels are associated with grain boundaries, surface scratches, amorphous regions or other defects that reduce the crystal quality yielding less clear diffraction patterns. So this map gives information about the microstructure of the film. It is composed by elongated grains, clearly visible in the IPF maps of Y and Z axes. So, in agreement with XRD measurements, laser-irradiation is inducing a preferential crystallographic orientation in the layer. This is, [001] is found in the plane of the layer, and elongated grains are formed growing almost parallel to the overlapping direction. It has to be said that some misalignment is visible if the grow direction of the elongated grains is closely inspected, so [001] crystallographic direction is not strictly perpendicular to the scan direction but always close to it.

In order to determine which parameter (scan direction or laser polarization) is affecting more this preferential orientation, two experiments have been designed, in which the scan direction has been changed but keeping the laser polarization the same. First, the scan direction (and consequently, overlapping direction) has been rotated 90°, as shown in Fig. 9e. Second, two consecutive areas have been irradiated, the second (scan direction parallel to Y-axis) covering part of the first (scan direction parallel to X-axis), as indicated in Fig. 9f. The EBSD results obtained for these two experiments are also presented in Fig. 9e-f. From these results, two conclusions can be extracted. First, the [001] crystallographic direction mainly remains in the XY plane, aligned with the overlap-

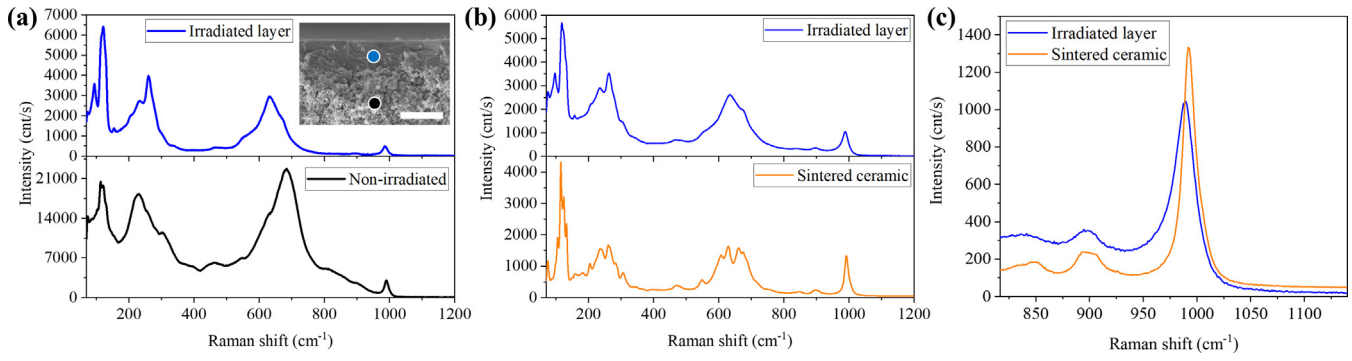

Fig. 8. µRaman spectra recorded on different samples ($\lambda_{exc} = 633nm$): (a) spectra recorded on the cross-section of the irradiated layer (blue line) and on the material below (black line). The inset shows a SEM image, indicating the points where the spectra were taken (scale bar of 15 µm). (b) Comparison of the spectra recorded on the irradiated layer (blue line) an on the sintered ceramic at 1450 °C (orange line). (c) Comparison of the Raman mode obtained at 993 cm^{-1} for the sintered ceramic and the irradiated layer.

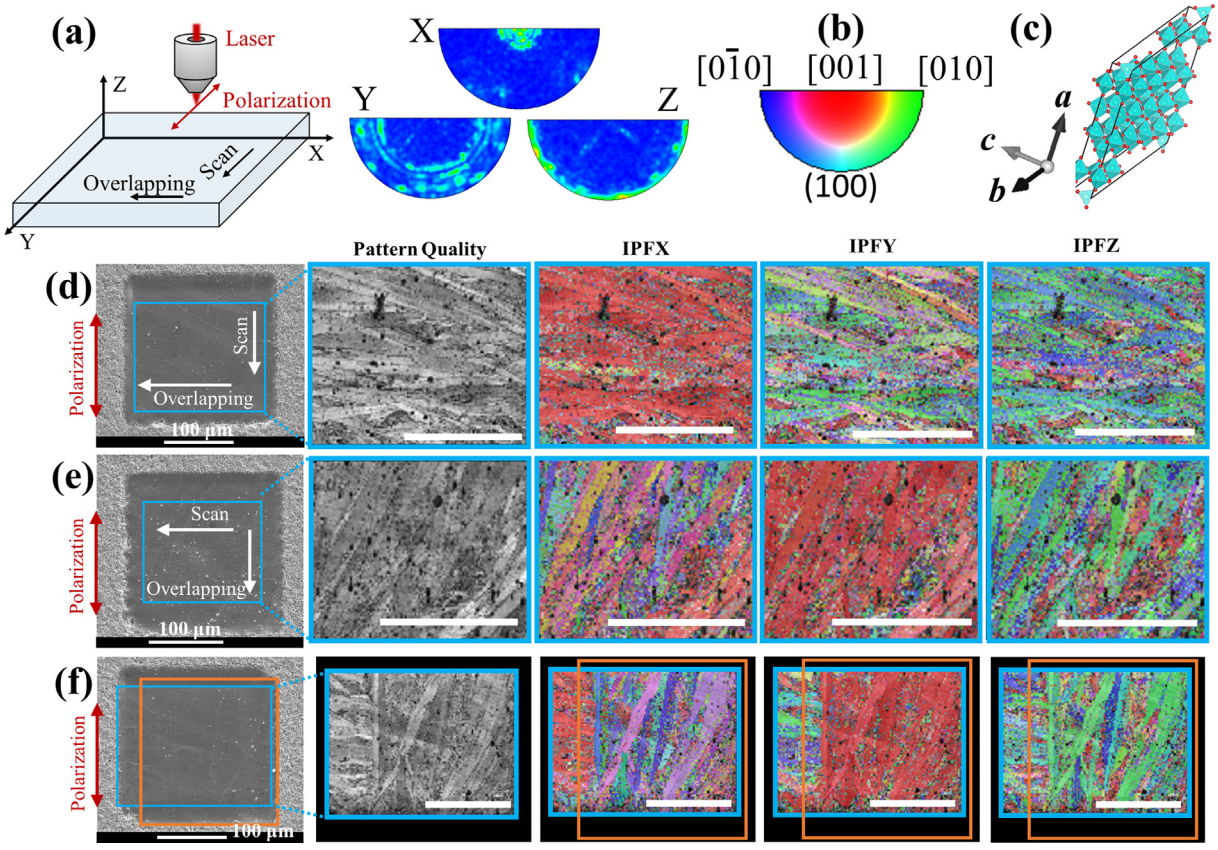

Fig. 9. EBSD measurements performed on different laser-irradiated areas (all the scale bars correspond to 100 µm). (a) Reference coordinate system used in the EBSD measurements respect to the layer orientation and Inverse Pole Figure (IPF) measured on an irradiated layer. (b) Inverse pole figure (IPF) with the colour correspondence of crystal orientation. (c) Crystal structure of monoclinic niobium oxide, indicating the crystallographic axes. (d) – (e) SEM image, pattern quality map and IPF maps for areas irradiated with different scan directions. (d) Scan direction along y-axis and overlapping direction along x-axis; (e) scan direction along x-axis and overlapping direction along y-axis; (f) two consecutive areas on the same region irradiated with different geometries: the second (scan direction parallel to Y-axis) covering part of the first (scan direction parallel to X-axis). The second area is indicated with an orange square.

ping direction, and the elongated grains grow along this direction. Then, it can be inferred that the overlapping direction mainly determines the orientation at which [001] is found, something that is related to in plane heat diffusion upon laser scanning. Second, the overlapping direction of the last irradiation and associated heat flow process is what determines the microstructure and crystal orientation in the laser-irradiated layer. This is clearly inferred from the results presented in Fig. 9f: first irradiation produces horizontal elongated grains; second irradiation induces vertical grains.

Similar preferential crystal orientation induced by ultrafast-laser irradiation has been described in other materials with crystal anisotropy [68–71]. In the Nb_2O_5 layers obtained in this work, a 2D crystalline area has been obtained with an alignment of the c-axis (short axis of the monoclinic structure) with the overlapping direction of the successive scans. This means that the elongated grains grow along the c-axis, which is the typical growth direction observed for Nb_2O_5 crystals [72,73]. Then, the preferential orientation is determined by the temperature gradients induced during the laser-irradiation process, as proposed by C. Fan et al. [74]. In the irradiation strategy reported here, an initial temperature gradient is produced along the scan direction, but then a gradient is established in the direction of overlapping scans. As we are working with highly overlapping scans, this second gradient is the one that mainly affects the crystal growth. This is, the first scan induces the formation of several crystallites that can act as seeds for the subsequent growth of the grains, whereas the overlapping scans generate a temperature gradient that promotes the growth of the grains along the short axis of the monoclinic structure (c-axis in Fig. 9c).

3.6. Electrical measurements

Finally, the electrical properties of the laser-irradiated layer have been studied. This will allow us to determine the effect of the generated defects and the microstructure on the electrical conductivity. Oxygen deficiency has a great impact on the electrical properties of Nb_2O_5. As it has been described before, the appearance of oxygen vacancies creates donor levels in the bandgap of the material, and, besides that, oxygen deficiency promotes the formation of cations with lower oxidation state (Nb^{4+}, Nb^{2+}) and hence an increase in the number of electrons available for conduction in the material is produced.

In principle, electrical resistivity for stoichiometric Nb_2O_5 can be as high as $10^9\ \Omega \cdot cm$ [24], which is a handicap for its use in electrical applications, as for example energy storage (batteries, supercapacitors...) where a minimum level of conductivity is required. Several works report on a considerable improvement of the conductivity of niobium oxides when a certain oxygen deficiency is present. For example, resistivity in the order of $10^5\ \Omega \cdot cm$ have been obtained for $Nb_{12}O_{29}$ and $Nb_{25}O_{62}$ [24], or even values in the range of 10^{-1} to $10^{-3}\ \Omega \cdot cm$ have been reported for $Nb_{25}O_{62}$, $Nb_{22}O_{54}$ or $Nb_{12}O_{29}$ [75]. $Nb_{12}O_{29}$ grown as thin film has been proposed as transparent conducting oxide with a resistivity of $3.3 \cdot 10^{-3}\ \Omega \cdot cm$ [76,77].

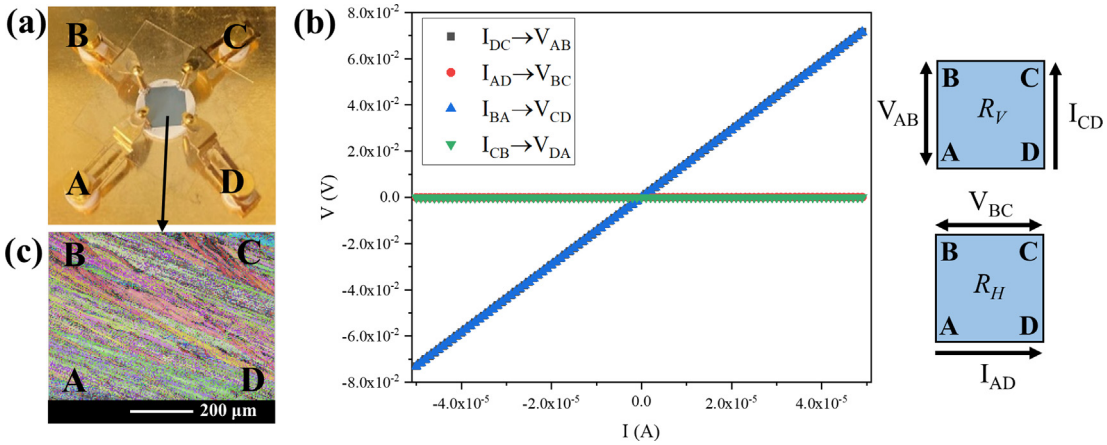

Fig. 10. Electrical conductivity measurements performed on laser-irradiated layers. (a) Sample mounted in a four-point probe system (Van der Pauw configuration). Each probe is labelled with a letter. (b) IV curves measured between pairs of contacts, as indicated in the figures on the right. (c) IPFY map for EBSD measurements done on a region of the sample shown in (a). The localization of the probes labelled in (a) are indicated in the map.

To study the electrical behaviour of the laser-irradiated layer (unpolished), a four-point probe system have been used with a Van der Pauw configuration (Fig. 10a). The four probes have been placed at the corners of the layer, and they have been labelled with A, B, C and D letters. In this configuration, a current is introduced between two consecutive probes and the potential drop is measured between the opposite two probes, as shown in the graph of Fig. 10b. I-V curves have been measured and are shown in Fig. 10b. It can be seen that the slope (i.e. R_V) of the curves for the potentials measured between AB and between CD are overlapping. The same situation is observed for the potential between AD and BC, but for this second pairs the slope (i.e. R_H) is much lower. That is, the resistance in the vertical direction (R_V) is higher than in the horizontal direction (R_H), indicating that the layer is anisotropic. This behaviour is in agreement with the microstructure of the layer observed by EBSD measurements, i.e., the resistance is higher across the grain boundaries than along the elongated grains (see Fig. 10c).

Van der Pauw theory [44,78] for calculating the resistivity of a sample considers that the sample is isotropic. Using the mathematical formalism derived by Van der Pauw (see supplementary section S1.1), a first estimation of the mean in-plane resistivity has been done for the Nb_2O_5 layers. For the different samples tested (those shown in Table 1) the in-plane resistivity value obtained is in the range 0.4 – 0.6 $\Omega \cdot cm$. This first estimation of the resistivity point towards a clear improvement on the conductivity of the layers of Nb_2O_5 obtained by ultrafast laser irradiation.

However, as it has been determined with the measurements shown in Fig. 10, it is better to treat the irradiated layer as an anisotropic media. To account for this anisotropy, the Montgomery method [79,80] has been applied to estimate the in-plane resistivities ρ_V and ρ_H. This method can be applied to anisotropic samples with parallelepipedic shape, and it is based on the transformation of the anisotropic to the isotropic equivalent sample [80] (see supplementary section S1.2). By performing the calculations, the in-plane resistivity values obtained are in the following ranges for all the samples tested in the optimal processing window:

$$\rho_V = [1.1, 1.6]\ \Omega \cdot cm$$

$$\rho_H = [0.2, 0.3]\ \Omega \cdot cm$$

As expected from the EBSD measurements, laser processing induces a controllable anisotropy with $\rho_V > \rho_H$. This is, electrons traveling in the horizontal direction of the elongated grains will experience lower resistivity than the electrons that have to cross the grain boundaries. Voids or cracks affecting the values of resistivity have been discarded by the SEM observations. It has to be pointed out that the resistance of a finite sample measured in a 4-point probe system with a square configuration is highly sensitive to the resistivity of the film[44]. Moderate values of resistivity anisotropy will produce high resistance anisotropy, in agreement with the measurements shown in Fig. 10b. The induced anisotropy could be useful for electrochemical sensors or solar cells [81], exploiting the chemical stability, corrosion resistance and biocompatibility of Nb_2O_5.

More relevant is the order of magnitude obtained for the resistivity. Both untreated and sintered pellets show a high isotropic resistivity. The measured value for the thermally sintered pellets is around $3{\cdot}10^8\ \Omega \cdot cm$, hence, the resistivity values obtained for the irradiated samples are about eight to nine orders of magnitude lower than in the sintered Nb_2O_5 (and equivalently, the conductivity is increased in that order of magnitude). The main reason behind this improvement in the electrical resistivity is the oxygen-deficiency of the material, as proven by XPS and Raman measurements. The obtained values present also a clear improvement respect to those previously reported in the literature for oxygen-deficient niobium oxides [24,75].

From the precedent discussion, it is clear that ultrafast laser irradiation can be used to fabricate Nb_2O_5 layers with highly improved conductivity due to the oxygen-deficiency, which retain the high temperature monoclinic phase as crystal structure. These results can be interesting for future electrical applications in energy storage devices, sensing or even in photocatalysis [4,7,14,18]. Moreover, the adaptability of laser powder bed processing to fabricate 3D architectures can be exploit to optimize the use of the material in sensors or energy storage electrodes [82,83]. Further controllability and improvement of the electrical properties of the material could be gained by the incorporation of dopants[4], which is feasible with the laser processing approach developed in this study. Future work will focus on the improvement of the mechanical properties and generated internal stresses in the ceramic layers.

4. Conclusions

In this work, sintered layers of high temperature monoclinic Nb_2O_5 have been produced by ultrafast-laser powder bed processing. The laser irradiation conditions have been optimized to obtain uniform and compact layers. More interestingly, these layers can

be produced in a few seconds and with very low power consumption, which is a clear improvement with respect the sintering of Nb_2O_5 by thermal treatment. The layers show a preferential crystal orientation with the short axis of the monoclinic structure contained in the plane of the layer. This preferential orientation can be controlled by the laser irradiation conditions.

The rapid rate of heating and cooling induced by the fs-laser irradiation is responsible for the stabilization of the high temperature crystal structure of Nb_2O_5. Intrinsic defects, mainly related to an oxygen deficiency induced by the laser-treatment, and the subsequent formation of Nb^{4+} and Nb^{2+} species, have a clear impact on the electrical properties of the material. Anisotropic behaviour of the electrical conductivity has been observed and related to the microstructure of the layers. Moreover, this microstructure can be controlled by the laser-processing conditions, which, combined with observed enhancement of several orders of magnitude of the electrical conductivity and the adaptability of the laser powder bed processing, will be really useful for designing materials and 3D networks to have optimal properties for energy storage, sensing or photocatalysis, among other applications.

CRediT authorship contribution statement

B. Sotillo: Conceptualization, Methodology, Software, Validation, Formal analysis, Investigation, Data curation, Writing – original draft, Writing – review & editing, Visualization, Project administration, Funding acquisition, Supervision. **R. Ariza:** Methodology, Software, Investigation, Writing – review & editing, Visualization, Validation. **P. Fernández:** Conceptualization, Validation, Resources, Writing – review & editing, Visualization, Project administration, Funding acquisition. **J. Solis:** Conceptualization, Validation, Resources, Writing – review & editing, Visualization, Project administration, Funding acquisition.

Data availability

Data will be made available on request.

Declaration of Competing Interest

The authors declare that they have no known competing financial interests or personal relationships that could have appeared to influence the work reported in this paper.

Acknowledgements

The authors are grateful to the Comunidad de Madrid for support via the Project PR65/19-22464 (Proyectos de I+D para jóvenes doctores) and MCIN/AEI/10.13039/501100011033 for the financial support through grant PID2020-112770RB-C21. This work has also been funded by Complutense University of Madrid and Banco Santander via the project UCM-Santander 2019 (PR87/19-22613). B. Sotillo acknowledges financial support from Comunidad de Madrid (Ayudas del Programa de Atracción de Talento 2017-T2/IND-5465). We acknowledge the Technical Services of CENIM-CSIC for the XPS measurements.

Appendix A. Supplementary material

Supplementary data to this article can be found online at https://doi.org/10.1016/j.matdes.2022.111346.

References

[1] C. Nico, T. Monteiro, M.P.F. Graça, Niobium oxides and niobates physical properties: Review and prospects, Prog. Mater. Sci. 80 (2016) 1–37, https://doi.org/10.1016/j.pmatsci.2016.02.001.
[2] M. Lübke, A. Sumboja, I.D. Johnson, D.J.L. Brett, P.R. Shearing, Z. Liu, J.A. Darr, High power nano-Nb2O5 negative electrodes for lithium-ion batteries, Electrochim. Acta 192 (2016) 363–369, https://doi.org/10.1016/J.ELECTACTA.2016.01.226.
[3] J. Wang, G. Li, D. Luo, Y. Zhang, Y. Zhao, G. Zhou, L. Shui, X. Wang, Z. Chen, Engineering the Conductive Network of Metal Oxide-Based Sulfur Cathode toward Efficient and Longevous Lithium-Sulfur Batteries, Adv. Energy Mater. 10 (2020) 2002076. doi.org/10.1002/aenm.202002076.
[4] Y. Yang, J. Zhao, Wadsley-Roth Crystallographic Shear Structure Niobium-Based Oxides: Promising Anode Materials for High-Safety Lithium-Ion Batteries, Adv. Sci. 8 (12) (2021) 2004855.
[5] T. Li, G. Nam, K. Liu, J.H. Wang, B. Zhao, Y. Ding, L. Soule, M. Avdeev, Z. Luo, W. Zhang, T. Yuan, P. Jing, M.G. Kim, Y. Song, M. Liu, A niobium oxide with a shear structure and planar defects for high-power lithium ion batteries, Energy Environ. Sci. 15 (2022) 254–264, https://doi.org/10.1039/d1ee02664j.
[6] Z. Tong, R. Yang, S. Wu, D. Shen, T. Jiao, K. Zhang, W. Zhang, C.-S. Lee, Surface-Engineered Black Niobium Oxide@Graphene Nanosheets for High-Performance Sodium-/Potassium-Ion Full Batteries, Small 15 (2019) 1901272. doi.org/10.1002/smll.201901272.
[7] K. Su, H. Liu, Z. Gao, P. Fornasiero, F. Wang, Nb2O5-Based Photocatalysts, Adv. Sci. 8 (2021) 2003156, https://doi.org/10.1002/ADVS.202003156.
[8] R.A. Rani, A.S. Zoolfakar, J.Z. Oua, M.R. Field, M. Austin, K. Kalantar-Zadeh, Nanoporous Nb2O5 hydrogen gas sensor, Sens. Actuators B Chem. 176 (2013) 149–156, https://doi.org/10.1016/J.SNB.2012.09.028.
[9] Y. De Wang, L.F. Yang, Z.L. Zhou, Y.F. Li, X.H. Wu, Effects of calcining temperature on lattice constants and gas-sensing properties of Nb2O5, Mater. Lett. 49 (2001) 277–281, https://doi.org/10.1016/S0167-577X(00)00384-0.
[10] Z. Zhou, M. Yang, Z. Fu, H. Wang, X. Ma, H. Gao, Electrode-induced polarity conversion in Nb 2 O 5 /NbO x resistive switching devices, Appl. Phys. Lett. 117 (24) (2020) 243502.
[11] O. Balci, E.O. Polat, N. Kakenov, C. Kocabas, Graphene-enabled electrically switchable radar-absorbing surfaces, Nat. Commun. 6 (2015) 6628, https://doi.org/10.1038/ncomms7628.
[12] M. Zhang, M.S. Cao, J.C. Shu, W.Q. Cao, L. Li, J. Yuan, Electromagnetic absorber converting radiation for multifunction, Mater. Sci. Eng. R Reports. 145 (2021), https://doi.org/10.1016/j.mser.2021.100627 100627.
[13] T.F. Yi, H.M.K. Sari, X. Li, F. Wang, Y.R. Zhu, J. Hu, J. Zhang, X. Li, A review of niobium oxides based nanocomposites for lithium-ion batteries, sodium-ion batteries and supercapacitors, Nano Energy. 85 (2021), https://doi.org/10.1016/j.nanoen.2021.105955 105955.
[14] L. Wang, X. Xie, K.N. Dinh, Q. Yan, J. Ma, Synthesis, characterizations, and utilization of oxygen-deficient metal oxides for lithium/sodium-ion batteries and supercapacitors, Coord. Chem. Rev. 397 (2019) 138–167, https://doi.org/10.1016/j.ccr.2019.06.015.
[15] D. Zu, H. Wang, S. Lin, G. Ou, H. Wei, S. Sun, H. Wu, Oxygen-deficient metal oxides: Synthesis routes and applications in energy and environment, Nano Res. (2019) 1–14.
[16] C. Dong, W. Dong, X. Lin, Y. Zhao, R. Li, F. Huang, Recent progress and perspectives of defective oxide anode materials for advanced lithium ion battery, EnergyChem. 2 (6) (2020) 100045.
[17] Y. Huang, Y. Yu, Y. Yu, B. Zhang, Oxygen Vacancy Engineering in Photocatalysis, Sol. RRL. 4 (2020) 2000037. doi.org/10.1002/solr.202000037.
[18] C. Zhang, G. Liu, X. Geng, K. Wu, M. Debliquy, Metal oxide semiconductors with highly concentrated oxygen vacancies for gas sensing materials: A review, Sensors Actuators, A Phys. 309 (2020), https://doi.org/10.1016/j.sna.2020.112026 112026.
[19] W. Zhao, W. Zhao, G. Zhu, T. Lin, F. Xu, F. Huang, Black Nb2O5 nanorods with improved solar absorption and enhanced photocatalytic activity, Dalt. Trans. 45 (2016) 3888–3894, https://doi.org/10.1039/C5DT04578A.
[20] S. Zhang, G. Liu, W. Qiao, J. Wang, L. Ling, Oxygen vacancies enhance the lithium ion intercalation pseudocapacitive properties of orthorhombic niobium pentoxide, J. Colloid Interface Sci. 562 (2020) 193–203, https://doi.org/10.1016/j.jcis.2019.12.015.
[21] Q. Wang, S. Zhang, H. He, C. Xie, Y. Tang, C. He, M. Shao, H. Wang, Oxygen Vacancy Engineering in Titanium Dioxide for Sodium Storage, Chem. – An Asian J. 16 (2021) 3–19. doi.org/10.1002/asia.202001172.
[22] R. Kashfi-Sadabad, S. Yazdani, T.D. Huan, Z. Cai, M.T. Pettes, Role of Oxygen Vacancy Defects in the Electrocatalytic Activity of Substoichiometric Molybdenum Oxide, J. Phys. Chem. C. 122 (2018) 18212–18222, https://doi.org/10.1021/acs.jpcc.8b03536.
[23] S. Bandi, A.K. Srivastav, Review: Oxygen-deficient tungsten oxides, J. Mater. Sci. 56 (2021) 6615–6644, https://doi.org/10.1007/s10853-020-05757-2.
[24] R. Li, Y. Qin, X. Liu, L. Yang, C. Lin, R. Xia, S. Lin, Y. Chen, J. Li, Conductive Nb25O62 and Nb12O29 anode materials for use in high-performance lithium-ion storage, Electrochim. Acta. 266 (2018) 202–211, https://doi.org/10.1016/j.electacta.2018.02.034.
[25] W.S. Liu, M.W. Liao, S.H. Huang, Y.I.A. Reyes, H.Y. Tiffany Chen, T.P. Perng, Formation and characterization of gray Ta2O5 and its enhanced photocatalytic

hydrogen generation activity, Int. J. Hydrogen Energy. 45 (2020) 16560–16568, https://doi.org/10.1016/j.ijhydene.2020.04.154.
[26] X. Mu, Q. Wen, G. Ou, Y. Du, P. He, M. Zhong, H. Zhu, H. Wu, S. Yang, Y. Liu, B. Li, X. Zhang, H. Zhou, A current collector covering nanostructured villous oxygen-deficient NiO fabricated by rapid laser-scan for Li-O2 batteries, Nano Energy. 51 (2018) 83–90, https://doi.org/10.1016/j.nanoen.2018.06.043.
[27] Y. Zhou, C.-K. Dong, Li−Li Han, J. Yang, X.-W. Du, Top-Down Preparation of Active Cobalt Oxide Catalyst, ACS Catal. 6 (10) (2016) 6699–6703.
[28] H. Palneedi, J.H. Park, D. Maurya, M. Peddigari, G.-T. Hwang, V. Annapureddy, J.-W. Kim, J.-J. Choi, B.-D. Hahn, S. Priya, K.J. Lee, J. Ryu, Laser Irradiation of Metal Oxide Films and Nanostructures: Applications and Advances, Adv. Mater. 30 (2018) 1705148. doi.org/10.1002/adma.201705148.
[29] K.C. Phillips, H.H. Gandhi, E. Mazur, S.K. Sundaram, Ultrafast laser processing of materials: a review, Adv. Opt. Photonics. 7 (2015) 684–712, https://doi.org/10.1364/AOP.7.000684.
[30] K. Sugioka, Y.a. Cheng, Ultrafast lasers-reliable tools for advanced materials processing, Light Sci. Appl. 3 (4) (2014) e149–e.
[31] K. Naito, M. Tsuneo, Review on Phase Equilibria and Defect Structures, Solid State Ionics. 12 (1984) 125–134.
[32] K.T. Jacob, C. Shekhar, M. Vinay, Y. Waseda, Thermodynamic properties of niobium oxides, J. Chem. Eng. Data. 55 (2010) 4854–4863, https://doi.org/10.1021/je1004609.
[33] N.M. Ferreira, M.C. Ferro, M.P.F. Graça, F.M. Costa, Effect of laser irradiation on lithium niobate powders, Ceram. Int. 43 (2017) 2504–2510, https://doi.org/10.1016/J.CERAMINT.2016.11.051.
[34] T. Le Mercier, J.M. Mariot, F. Goubard, M. Quarton, M.F. Fontaine, C.F. Hague, Structural and chemical transformations induced by laser impact on TiO2 and Nb2O5, J. Phys. Chem. Solids. 58 (1997) 679–684, https://doi.org/10.1016/S0022-3697(96)00196-5.
[35] D. Grossin, A. Montón, P. Navarrete-Segado, E. Özmen, G. Urruth, F. Maury, D. Maury, C. Frances, M. Tourbin, P. Lenormand, G. Bertrand, A review of additive manufacturing of ceramics by powder bed selective laser processing (sintering / melting): Calcium phosphate, silicon carbide, zirconia, alumina, and their composites, Open Ceram. 5 (2021), https://doi.org/10.1016/J.OCERAM.2021.100073 100073.
[36] S. Pfeiffer, K. Florio, D. Puccio, M. Grasso, B.M. Colosimo, C.G. Aneziris, K. Wegener, T. Graule, Direct laser additive manufacturing of high performance oxide ceramics: A state-of-the-art review, J. Eur. Ceram. Soc. 41 (2021) 6087–6114, https://doi.org/10.1016/j.jeurceramsoc.2021.05.035.
[37] S.L. Sing, W.Y. Yeong, F.E. Wiria, B.Y. Tay, Z.Q. Zhao, L. Zhao, Z.L. Tian, S.F. Yang, Direct selective laser sintering and melting of ceramics: a review, Rapid Prototyp. J. 23 (2017) 611–623, https://doi.org/10.1108/RPJ-11-2015-0178.
[38] Y. Wu, Y. Chen, L. Kong, Z. Jing, X. Liang, A Review on Ultrafast-Laser Power Bed Fusion Technology, Crystals. 12 (2022) 1480. www.mdpi.com/2073-4352/12/10/1480.
[39] K. Florio, S. Pfeiffer, M. Makowska, N. Casati, F. Verga, T. Graule, H. Van Swygenhoven, K. Wegener, An Innovative Selective Laser Melting Process for Hematite-Doped Aluminum Oxide, Adv. Eng. Mater. 21 (2019), https://doi.org/10.1002/ADEM.201801352/FORMAT/PDF.
[40] T. Ullsperger, D. Liu, B. Yürekli, G. Matthäus, L. Schade, B. Seyfarth, H. Kohl, R. Ramm, M. Rettenmayr, S. Nolte, Ultra-short pulsed laser powder bed fusion of Al-Si alloys: Impact of pulse duration and energy in comparison to continuous wave excitation, Addit. Manuf. 46 (2021), https://doi.org/10.1016/J.ADDMA.2021.102085 102085.
[41] R. Ariza, M. Alvarez-Alegria, G. Costas, L. Tribaldo, A.R. Gonzalez-Elipe, J. Siegel, J. Solis, Multiscale ultrafast laser texturing of marble for reduced surface wetting, Appl. Surf. Sci. 577 (2022) 151850.
[42] E. de Prado, C. Florian, B. Sotillo, J. Siegel, J. Solis, P. Fernández, Optical spectroscopy study of nano- and microstructures fabricated by femtosecond laser pulses on ZnO based systems, CrystEngComm. 20 (2018) 2952–2960, https://doi.org/10.1039/C8CE00436F.
[43] https://web.archive.org/web/20060615044930/http://www.eeel.nist.gov/812/hall.html.
[44] I. Miccoli, F. Edler, H. Pfnür, C. Tegenkamp, The 100th anniversary of the four-point probe technique: the role of probe geometries in isotropic and anisotropic systems, J. Phys. Condens. Matter. 27 (22) (2015) 223201.
[45] J.P. Oliveira, A.D. LaLonde, J. Ma, Processing parameters in laser powder bed fusion metal additive manufacturing, Mater. Des. 193 (2020) 1–12, https://doi.org/10.1016/j.matdes.2020.108762.
[46] J.P. Oliveira, Z. Zeng, T. Omori, N. Zhou, R.M. Miranda, F.M.B. Fernandes, Improvement of damping properties in laser processed superelastic Cu-Al-Mn shape memory alloys, Mater. Des. 98 (2016) 280–284, https://doi.org/10.1016/j.matdes.2016.03.032.
[47] S.M. Eaton, H. Zhang, P.R. Herman, F. Yoshino, L. Shah, J. Bovatsek, A.Y. Arai, Heat accumulation effects in femtosecond laser-written waveguides with variable repetition rate, Opt. Express. 13 (2005) 4708–4716, https://doi.org/10.1364/OPEX.13.004708.
[48] L. Mitterhuber, E. Kraker, S. Defregger, Structure Function Analysis of Temperature-Dependent Thermal Properties of Nm-Thin Nb2O5, Energies. 12 (4) (2019) 610.
[49] O.B. Shcherbina, M.N. Palatnikov, V.V. Efremov, Mechanical properties of Nb 2O 5 and Ta 2O 5 prepared by different procedures, Inorg. Mater. 48 (2012) 433–438, https://doi.org/10.1134/S0020168512040139.
[50] V. Augustyn, J. Come, M.A. Lowe, J.W. Kim, P.-L. Taberna, S.H. Tolbert, H.D. Abruña, P. Simon, B. Dunn, High-rate electrochemical energy storage through Li+ intercalation pseudocapacitance, Nat. Mater. 12 (2013) 518–522, https://doi.org/10.1038/nmat3601.
[51] Y.u. Wang, X. Fu, M. Zheng, W.-H. Zhong, G. Cao, Strategies for Building Robust Traffic Networks in Advanced Energy Storage Devices: A Focus on Composite Electrodes, Adv. Mater. 31 (6) (2019) 1804204.
[52] H. Schäfer, R. Gruehn, F. Schulte, The Modifications of Niobium Pentoxide, Angew. Chemie Int. Ed. English. 5 (1966) 40–52, https://doi.org/10.1002/anie.196600401.
[53] M.T. Greiner, L. Chai, M.G. Helander, W.-M. Tang, Z.-H. Lu, Transition Metal Oxide Work Functions: The Influence of Cation Oxidation State and Oxygen Vacancies, Adv. Funct. Mater. 22 (2012) 4557–4568. doi.org/10.1002/adfm.201200615.
[54] Z. Weibin, W. Weidong, W. Xueming, C. Xinlu, Y. Dawei, S. Changle, P. Liping, W. Yuying, B. Li, The investigation of NbO2 and Nb2O5 electronic structure by XPS, UPS and first principles methods, Surf. Interface Anal. 45 (2013) 1206–1210, https://doi.org/10.1002/SIA.5253/FORMAT/PDF.
[55] H.D. Asfaw, C.W. Tai, L. Nyholm, K. Edström, Over-Stoichiometric NbO2 Nanoparticles for a High Energy and Power Density Lithium Microbattery, ChemNanoMat. 3 (2017) 646–655, https://doi.org/10.1002/cnma.201700141.
[56] W. Zhang, L. Cai, S. Cao, L. Qiao, Y.i. Zeng, Z. Zhu, Z. Lv, H. Xia, L. Zhong, H. Zhang, X. Ge, J. Wei, S. Xi, Y. Du, S. Li, X. Chen, Interfacial lattice-strain-driven generation of oxygen vacancies in an aerobic-annealed TiO2(B) electrode, Adv. Mater. 31 (52) (2019) 1906156.
[57] V.V. Atuchin, I.E. Kalabin, V.G. Kesler, N.V. Pervukhina, Nb 3d and O 1s core levels and chemical bonding in niobates, J. Electron Spectros. Relat. Phenomena. 142 (2005) 129–134, https://doi.org/10.1016/J.ELSPEC.2004.10.003.
[58] K. Momma, F. Izumi, VESTA 3 for three-dimensional visualization of crystal, volumetric and morphology data, J. Appl. Crystallogr. 44 (2011) 1272–1276, https://doi.org/10.1107/S0021889811038970.
[59] A.A. McConnell, J.S. Aderson, C.N.R. Rao, Raman spectra of niobium oxides, Spectrochim. Acta Part A Mol. Spectrosc. 32 (1976) 1067–1076, https://doi.org/10.1016/0584-8539(76)80291-7.
[60] T. Ikeya, M. Senna, Change in the structure of niobium pentoxide due to mechanical and thermal treatments, J. Non. Cryst. Solids. 105 (1988) 243–250, https://doi.org/10.1016/0022-3093(88)90313-4.
[61] J.M. Jehng, I.E. Wachs, Structural chemistry and Raman spectra of niobium oxides, Chem. Mater. 3 (1991) 100–107, https://doi.org/10.1021/cm00013a025.
[62] S. Andersson, J. Galy, Wadsley defects and crystallographic shear in hexagonally close-packed structures, J. Solid State Chem. 1 (1970) 576–582, https://doi.org/10.1016/0022-4596(70)90144-1.
[63] M.P.F. Graça, A. Meireles, C. Nico, M.A. Valente, Nb2O5 nanosize powders prepared by sol–gel – Structure, morphology and dielectric properties, J. Alloys Compd. 553 (2013) 177–182, https://doi.org/10.1016/J.JALLCOM.2012.11.128.
[64] J.R. McBride, K.C. Hass, B.D. Poindexter, W.H. Weber, Raman and x-ray studies of Ce1−xRExO2−y, where RE=La, Pr, Nd, Eu, Gd, and Tb, J. Appl. Phys. 76 (1994) 2435–2441, https://doi.org/10.1063/1.357593.
[65] M. Salari, K. Konstantinov, H.K. Liu, Enhancement of the capacitance in TiO2 nanotubes through controlled introduction of oxygen vacancies, J. Mater. Chem. 21 (2011) 5128–5133, https://doi.org/10.1039/C0JM04085A.
[66] K. Ye, K. Li, Y. Lu, Z. Guo, N. Ni, H. Liu, Y. Huang, H. Ji, P. Wang, An overview of advanced methods for the characterization of oxygen vacancies in materials, TrAC - Trends Anal. Chem. 116 (2019) 102–108, https://doi.org/10.1016/j.trac.2019.05.002.
[67] F.D. Hardcastle, I.E. Wachs, Determination of niobium-oxygen bond distances and bond orders by Raman spectroscopy, Solid State Ionics 45 (1991) 201–213, https://doi.org/10.1016/0167-2738(91)90153-3.
[68] A. Stone, H. Jain, V. Dierolf, M. Sakakura, Y. Shimotsuma, K. Miura, K. Hirao, J. Lapointe, R. Kashyap, Direct laser-writing of ferroelectric single-crystal waveguide architectures in glass for 3D integrated optics, Sci. Rep. 5 (1) (2015).
[69] A. Stone, M. Sakakura, Y. Shimotsuma, K. Miura, K. Hirao, V. Dierolf, H. Jain, Femtosecond laser-writing of 3D crystal architecture in glass: Growth dynamics and morphological control, Mater. Des. 146 (2018) 228–238, https://doi.org/10.1016/J.MATDES.2018.03.016.
[70] X. He, C. Fan, B. Poumellec, Q. Liu, H. Zeng, F. Brisset, G. Chen, X. Zhao, M. Lancry, Size-controlled oriented crystallization in SiO2-based glasses by femtosecond laser irradiation (2014). https://doi.org/10.1364/JOSAB.31.000376.
[71] K. Veenhuizen, S. McAnany, D. Nolan, B. Aitken, V. Dierolf, H. Jain, Fabrication of graded index single crystal in glass, Sci. Rep. 7 (2017), https://doi.org/10.1038/srep44327.
[72] J. He, Y. Hu, Z. Wang, W. Lu, S. Yang, G. Wu, Y. Wang, S. Wang, H. Gu, J. Wang, Hydrothermal growth and optical properties of Nb2O5 nanorod arrays, J. Mater. Chem. C. 2 (2014) 8185–8190, https://doi.org/10.1039/C4TC01581A.
[73] B. Sotillo, F.A. López, L. Alcaraz, P. Fernández, Characterization of Nb22O54 microrods grown from niobium oxide powders recovered from mine tailings, Ceram. Int. 47 (10) (2021) 13859–13864.
[74] C. Fan, B. Poumellec, M. Lancry, X. He, H. Zeng, A. Erraji-Chahid, Q. Liu, G. Chen, Three-dimensional photoprecipitation of oriented LiNbO_3-like crystals in silica-based glass with femtosecond laser irradiation, Opt. Lett. 37 (2012) 2955, https://doi.org/10.1364/ol.37.002955.

[75] R.J. Cava, B. Batlogg, J.J. Krajewski, H.F. Poulsen, P. Gammel, W.F. Peck, L.W. Rupp, Electrical and magnetic properties of Nb2O5-δ crystallographic shear structures, Phys. Rev. B. 44 (1991) 6973–6981, https://doi.org/10.1103/PhysRevB.44.6973.
[76] T. Ohsawa, J. Okubo, T. Suzuki, H. Kumigashira, M. Oshima, T. Hitosugi, An n-type transparent conducting oxide: Nb12O29, J. Phys. Chem. C. 115 (2011) 16625–16629, https://doi.org/10.1021/jp203021u.
[77] T. Ohsawa, T. Suzuki, T. Hitosugi, High-temperature stability of Nb12O29 transparent conductor, Thin Solid Films. 526 (2012) 218–220, https://doi.org/10.1016/j.tsf.2012.11.025.
[78] F.S. Oliveira, R.B. Cipriano, F.T. da Silva, E.C. Romão, C.A.M. dos Santos, Simple analytical method for determining electrical resistivity and sheet resistance using the van der Pauw procedure, Sci. Rep. 10 (2020), https://doi.org/10.1038/s41598-020-72097-1.
[79] H.C. Montgomery, Method for Measuring Electrical Resistivity of Anisotropic Materials, J. Appl. Phys. 42 (1971) 2971–2975, https://doi.org/10.1063/1.1660656.
[80] C.A.M. Dos Santos, A. De Campos, M.S. Da Luz, B.D. White, J.J. Neumeier, B.S. De Lima, C.Y. Shigue, Procedure for measuring electrical resistivity of anisotropic materials: A revision of the Montgomery method, J. Appl. Phys. 110 (2011) 2975, https://doi.org/10.1063/1.3652905.
[81] C. Lopez-Santos, D. Puerto, J. Siegel, M. Macias-Montero, C. Florian, J. Gil-Rostra, V. López-Flores, A. Borras, A.R. González-Elipe, J. Solis, Anisotropic Resistivity Surfaces Produced in ITO Films by Laser-Induced Nanoscale Self-organization, Adv. Opt. Mater. 9 (2) (2021) 2001086.
[82] S. Chabi, C. Peng, D. Hu, Y. Zhu, S. Chabi, C. Peng, D. Hu, Y. Zhu, Ideal Three-Dimensional Electrode Structures for Electrochemical Energy Storage 1. Introduction, Adv. Mater. 26 (2014) 2440–2445, https://doi.org/10.1002/adma.201305095.
[83] Q. Xu, Y. Lv, C. Dong, T.S. Sreeprased, A. Tian, H. Zhang, Y. Tang, Z. Yu, N. Li, Three-dimensional micro/nanoscale architectures: fabrication and applications, Nanoscale. 7 (2015) 10883–10895, https://doi.org/10.1039/C5NR02048D.